Evolution from quantum anomalous Hall insulator to heavy-fermion semimetal in magic-angle twisted bilayer graphene

Cheng Huang,[1] Xu Zhang,[1] Gaopei Pan,[2,3] Heqiu Li,[4] Kai Sun,[5,*] Xi Dai,[6,†] and Zi Yang Meng[1,‡]

[1]*Department of Physics and HKU-UCAS Joint Institute of Theoretical and Computational Physics, The University of Hong Kong, Pokfulam Road, Hong Kong SAR, China*

[2]*Beijing National Laboratory for Condensed Matter Physics and Institute of Physics, Chinese Academy of Sciences, Beijing 100190, China*

[3]*School of Physical Sciences, University of Chinese Academy of Sciences, Beijing 100049, China*

[4]*Department of Physics, University of Toronto, Toronto, Ontario, Canada M5S 1A7*

[5]*Department of Physics, University of Michigan, Ann Arbor, Michigan 48109, USA*

[6]*Department of Physics, Hong Kong University of Science and Technology, Kowloon, Hong Kong SAR, China*

(Received 27 May 2023; accepted 9 February 2024; published 4 March 2024)

The ground states of twisted bilayer graphene (TBG) at chiral and flat-band limit with integer fillings are known from exact solutions, while their dynamical and thermodynamical properties are revealed by unbiased quantum Monte Carlo (QMC) simulations. However, to elucidate experimental observations of correlated metallic, insulating, and superconducting states and their transitions, investigations on realistic, or nonchiral cases are vital. Here we employ momentum-space QMC method to investigate the evolution of correlated states in magic-angle TBG away from chiral limit at charge neutrality with polarized spin/valley, which approximates to an experimental case with filling factor $\nu = -3$. We find that the ground state evolves from quantum anomalous Hall insulator into an intriguing correlated semimetallic state possessing heavy-fermion features as AA hopping strength reaches experimental values. Such a state resembles the recently proposed heavy-fermion representations with localized electrons residing at AA stacking regions and delocalized electrons itinerating via AB/BA stacking regions. The spectral signatures of the localized and itinerant electrons in the heavy-fermion semimetal phase are revealed, with the connection to experimental results being discussed.

DOI: 10.1103/PhysRevB.109.125404

I. INTRODUCTION

Flat bands of noninteracting magic-angle twisted bilayer graphene (TBG) can be readily characterized by tight-binding [1,2] and continuous Bistritzer-MacDonald [3] models. Yet, in such deceptively simple systems, it is the interplay of long-range Coulomb interaction, quantum metric of flat-band wave function and the extremely high tunability, by twisting angles, gating, and dielectric environment, that gives rise to a plethora of novel quantum states including correlated insulator [4–14], unconventional metal with linear-T resistivity, superconductor, and beyond [15–20], the underlying principles and mechanisms of which are still under intensive investigations.

Among these efforts, exact solutions [14,21–24], mean-field analyses [23,25–32], density matrix renormalization group (DMRG) investigations [33,34], and momentum-space quantum Monte Carlo (QMC) simulations [35–39] reveal that the TBG model of the first magic angle (1.08°) with Coulomb interaction projected into the flat bands possesses a quantum anomalous Hall (QAH) ground state with Chern number $C = 1$, at chiral (AA stacking hopping $u_0 = 0$) and flat-band limit (ignoring kinetic energy) with filling factor $\nu = \pm 3$ (which means one of the eight spin or valley degenerate bands are occupied for $\nu = -3$, or seven considering particle-hole symmetry for $\nu = 3$). For the same system away from chiral limit, which means $u_0 > 0$ (can be varied experimentally by twisting angle, temperature, strain, magnetic field, or pressure, etc. [16,18]), a DMRG investigation suggests its ground state remains Chern number polarized until $u_0/u_1 \approx 0.8$ (AB/BA stacking hopping $u_1 \approx 110\,\text{meV}$ [40–42]), beyond which competing states such as gapless $C_2\mathcal{T}$ nematic and gapped $C_2\mathcal{T}$ stripe phases emerge [33]. Nevertheless, another DMRG work indicates the ground state a nematic $C_2\mathcal{T}$ semimetal when $u_0/u_1 > 0.8$ [34], while a recent Hartree-Fock mean-field study suggests the corresponding state to be insulating and monolayer charge density modulated with $C_2\mathcal{T}$ symmetry [29].

Experimentally, magic-angle (hereafter magic angle refers to the first magic angle) TBG at $\nu = -3$ is found to be metallic (or semimetallic considering carrier concentration) with C_3 symmetric electron localization, neighboring to a superconducting phase, while that of $\nu = 3$ is semiconducting or insulating [6,8,9,11,43–45], when u_1 is around 110 meV [40–42] and u_0 around 0.8 of u_1 [8,46,47] due to lattice relaxation. The discrepancies between the experimental

*sunkai@umich.edu
†daix@ust.hk
‡zymeng@hku.hk

 ©2024 American Physical Society

observations (especially for $\nu = -3$) and the above theoretical proposals are intriguing.

To understand and clarify the discrepancies between theories and experiments, in this work, we apply the unbiased momentum-space QMC simulation [35–39,48], supplemented by exact diagonalization (ED) [49], to systematically investigate the evolution of the correlated states of magic-angle TBG at $\nu = -3$ and away from chiral limit (increasing u_0), with the Coulomb interaction projected into flat bands. Our results show the critical transition temperature (T_c) of the QAH state decreases with increasing u_0, and eventually vanish at $u_0 \approx 90$ meV, the approximate value of realistic u_0, where a semimetallic (SM) state probably preserving C_3 rotation symmetry emerges, as meanwhile the quasiparticle gap reduces to zero. This semimetallic state is gapless in the vicinity of Γ point of the moiré Brilliouin zone (mBZ). In real space it has localized states at the AA stacking region while itinerant states at the AB/BA stacking regions of the moiré unit cell (mUC), and the localized states and itinerant states are well separated in energy—an analog to the experiments [8,9] and recently found heavy-fermion representations of the TBG system, with AA stacking regions proposed to hold states of localized flat bands (f electrons) and AB/BA stacking regions bridging itinerant states (c electrons) [32,50–56].

Since our model has no prior heavy-fermion representation in the first place but mainly the approximation of projecting the Coulomb interaction into the flat bands, our observation, the evolution from QAH insulator to heavy-fermion semimetal at $\nu = -3$, provides an unbiased and unifying interpretation of the ground-state transition of magic-angle TBG from topological insulator (at chiral limit) to the SM state (nonchiral) with topological heavy-fermion features.

II. MODEL AND METHOD

The real-space moiré superlattice generated by TBG is shown in Fig. 7. In principle, the Hamiltonian of TBG contains kinetics and interaction, $H = H_0 + H_I$. The kinetic part is

$$H_0 = \sum_{\mathbf{k},\mathbf{G},\mathbf{G}',\eta,s} \mathbf{c}^\dagger_{\mathbf{k},\mathbf{G},\eta,s} H^{\eta,s}(\mathbf{k})_{\mathbf{G},\mathbf{G}'} \mathbf{c}_{\mathbf{k},\mathbf{G}',\eta,s}, \tag{1}$$

where

$$H^{\eta,s}(\mathbf{k})_{\mathbf{G},\mathbf{G}'} = \delta_{\mathbf{k}_1,\mathbf{k}_2} \hbar v_{\mathrm{F}} \begin{pmatrix} -(\mathbf{k}_1 - \mathbf{K}_1^\eta)\cdot\sigma^\eta & 0 \\ 0 & -(\mathbf{k}_1 - \mathbf{K}_2^\eta)\cdot\sigma^\eta \end{pmatrix} + \begin{pmatrix} 0 & T_1^\eta \\ T_2^{\eta\dagger} & 0 \end{pmatrix} \tag{2}$$

is the BM model [3] with

$$T_l^\eta = \begin{pmatrix} u_0 & u_1 \\ u_1 & u_0 \end{pmatrix} \delta_{\mathbf{k}_1,\mathbf{k}_2} + \begin{pmatrix} u_0 & u_1 \mathrm{e}^{-i\frac{2\pi}{3}\eta} \\ u_1 \mathrm{e}^{i\frac{2\pi}{3}\eta} & u_0 \end{pmatrix} \delta_{\mathbf{k}_1,\mathbf{k}_2+(-1)^l\eta\mathbf{G}_1} + \begin{pmatrix} u_0 & u_1 \mathrm{e}^{i\frac{2\pi}{3}\eta} \\ u_1 \mathrm{e}^{-i\frac{2\pi}{3}\eta} & u_0 \end{pmatrix} \delta_{\mathbf{k}_1,\mathbf{k}_2+(-1)^l\eta(\mathbf{G}_1+\mathbf{G}_2)}. \tag{3}$$

Here $\mathbf{k}$ is a momentum in mBZ, $\mathbf{G}$ is a momentum difference for $\mathbf{k}$, as $\mathbf{k}_1 = \mathbf{k} + \mathbf{G}$ and $\mathbf{k}_2 = \mathbf{k} + \mathbf{G}'$, to account for the contribution from extended Brillouin zones. $\mathbf{G}, \mathbf{G}' \in \{N_1\mathbf{G}_1 + N_2\mathbf{G}_2\}$, the combinations of lattices of mBZ, with N_1 and N_2 being integers, and a cutoff, $|\mathbf{G}|, |\mathbf{G}'| \leqslant 4|\mathbf{G}_1|$, is applied. $\mathbf{c}^\dagger_{\mathbf{k},\mathbf{G},\eta,s}$ is a 1×4 vector of creation operators, $c^\dagger_{\mathbf{k},\mathbf{G},\eta,s,X}$, where X is the index referring to layers and sublattices, as $X \in \{\mathrm{A}_1, \mathrm{B}_1, \mathrm{A}_2, \mathrm{B}_2\}$ for layers (1, 2) and sublattices (A, B). In addition, s specifies spins ($\uparrow, \downarrow$) and $\eta = \pm$ labels the two valleys. v_{F} is the Fermi velocity and we set $\hbar v_{\mathrm{F}}/(\sqrt{3}a) = 2.37745$ eV corresponding to flat bands, with a the distance of nearest carbon atoms. $\sigma^\eta = (\eta\sigma_x, \sigma_y)$, where σ_x and σ_y are Pauli matrices refer to sublattices. The first part of $H^{\eta,s}(\mathbf{k})_{\mathbf{G},\mathbf{G}'}$ stands for intralayer hopping of the top (1) layer and the bottom (2) layer, respectively, and the second part stands for interlayer hopping, which is actually the moiré potential.

The interaction part is of density-density, as

$$H_{\mathrm{I}} = \frac{1}{2\Omega} \sum_{\mathbf{q}\in\mathrm{mBZ},\mathbf{G}} V(\mathbf{q}+\mathbf{G}) \delta\rho_{\mathbf{q}+\mathbf{G}} \delta\rho_{-\mathbf{q}-\mathbf{G}}, \tag{4}$$

where

$$\delta\rho_{\mathbf{q}+\mathbf{G}} = \sum_{\mathbf{k},\mathbf{G}',\eta,s,X} \left(c^\dagger_{\mathbf{k},\mathbf{G}',\eta,s,X} c_{\mathbf{k}+\mathbf{q}+\mathbf{G},\mathbf{G}',\eta,s,X} - \frac{\nu+4}{8} \delta_{\mathbf{q},0} \delta_{\mathbf{G},0} \right). \tag{5}$$

Here $\delta\rho_{\mathbf{q}}$ is the electron density operator with the reference to $(\nu+4)/8$, where ν is the filling parameter with $\nu = 0$ as the charge neutrality. $V(\mathbf{q})$ is the long-range screened Coulombic interaction decaying as $V(\mathbf{q}) = \frac{\mathrm{e}^2}{2\varepsilon} \frac{1}{|\mathbf{q}|}(1 - \mathrm{e}^{-|\mathbf{q}|d})$ [38], where $d/2$ is the distance between TBG and a bottom gate [57] (here we set $d = 40$ nm) and ε ($= 7\ \varepsilon_0$) is the dielectric constant. The fermion momentum transfer, $\mathbf{q} + \mathbf{G}$, is cut off at the amplitude of $|\mathbf{G}_1|$. $\Omega = N_k |\mathbf{a}_{\mathrm{M}1}||\mathbf{a}_{\mathrm{M}2}|\sqrt{3}/2$ is the total area of moiré superlattice that we consider in real space, where $N_k = L \times L$ is the number of $\mathbf{k}$ points sampling in mBZ and L is the linear size, and $\mathbf{a}_{\mathrm{M}1}$ and $\mathbf{a}_{\mathrm{M}2}$ are the lattice vectors of mUC as shown in Fig. 7, with $|\mathbf{a}_{\mathrm{M}1/\mathrm{M}2}| = \sqrt{3}a/[2\sin(\theta/2)]$ and $\theta = 1.08°$, the twisting angle.

As shown in Fig. 8 in the Appendix, even in nonchiral cases ($u_0 > 0$), the two low-energy bands of H_0 are quite flat and isolated from the remote bands, except when $u_0 \approx u_1$ and $u_0 > 160$ meV. In these isolated flat-band cases, therefore, the low-energy physics of $H = H_0 + H_{\mathrm{I}}$ can be well captured by the two flat bands, and H can thus be projected onto them. Setting the eigenvalues and eigenvectors of $H^{\eta,s}(\mathbf{k})$ to be $\epsilon_m^{\eta,s}(\mathbf{k})$ and $|u_{\mathbf{k},m,\eta,s}\rangle$, where $m = \pm$ is the index for the flat bands, and projecting H onto the flat bands, as $c^\dagger_{\mathbf{k},m,\eta,s} = \sum_{\mathbf{G},X} c^\dagger_{\mathbf{k},\mathbf{G},\eta,s,X} |u_{\mathbf{k},m,\eta,s}\rangle_{\mathbf{G},X}$, yields

$$H_0 = \sum_{\mathbf{k},m,\eta,s} \epsilon_m^{\eta,s}(\mathbf{k}) c^\dagger_{\mathbf{k},m,\eta,s} c_{\mathbf{k},m,\eta,s},$$

$$H_{\mathrm{I}} = \frac{1}{2\Omega} \sum_{|\mathbf{q}+\mathbf{G}|\neq 0} V(\mathbf{q}+\mathbf{G}) \delta\rho_{\mathbf{q}+\mathbf{G}} \delta\rho_{-\mathbf{q}-\mathbf{G}}, \tag{6}$$

where $\delta\rho_{\mathbf{q}+\mathbf{G}} = \sum_{\mathbf{k},m_1,m_2,\eta,s} \lambda_{m_1,m_2,\eta,s}(\mathbf{k}, \mathbf{k}+\mathbf{q}+\mathbf{G})(c^\dagger_{\mathbf{k},m_1,\eta,s} c_{\mathbf{k}+\mathbf{q}+\mathbf{G},m_2,\eta,s} - \frac{\nu+4}{8} \delta_{\mathbf{q},0}\, \delta_{m_1,m_2})$, and the form factor $\lambda_{m_1,m_2,\eta,s}(\mathbf{k},\ \mathbf{k}+\mathbf{q}+\mathbf{G}) \equiv \langle\, u_{\mathbf{k},m_1,\eta,s} \mid u_{\mathbf{k}+\mathbf{q}+\mathbf{G},m_2,\eta,s}\,\rangle$. To efficiently simulate the system at filling $\nu = -3$, same as earlier studies [33,34], we take two half-filled flat bands of $\eta = +$ & $s = \uparrow$ into consideration due to its spin- and valley-polarized ground state [29,33,34], while other flat

bands of the rest combinations of spin and valley, which remain empty, can be safely ignored in the simulations. Note that we strip the indices of valley and spin, η and s, in the following. The above H is tackled by determinant QMC method, the detail of which is depicted in Appendix A. We would like to note that our simulation ingnores the kinetic term H_0, due to its flat dispersion, after the projection onto flat bands, thus corresponding to a perfect flat-band limit. Moreover, our model tends to predict the nature of pristine TBG and does not take any heterostrain into account, and therefore the incommensurate Kekule spiral state found in experiments [58–61] will not be detected.

III. RESULTS

The ground state of this system at chiral limit is found to be a Chern-number polarized QAH state [38]. To investigate if the QAH state sustains in nonchiral cases, the correlation of its QAH order is calculated. The QAH order parameter is defined as $P_C/N_\mathbf{k}$, where $P_C = N_+ - N_-$ and $N_m = \sum_\mathbf{k} c^\dagger_{\mathbf{k},m} c_{\mathbf{k},m}$, the occupation number operator of two flat bands. The correlation of this QAH order, or Chern-number polarization, is $S \equiv \langle (N_+ - N_-)^2 \rangle / N_\mathbf{k}^2$. Its T and u_0 dependence for $L = 4$ system is shown in Fig. 1(b). For specific u_0, S increases with decreasing T, which manifests spontaneous time-reversal symmetry breaking and a QAH ground state (a topological insulator) at low temperature [38,62,63]. For each fixed u_0, finite-size scaling is carried out to derive the T_c of the spontaneous time-reversal symmetry breaking of the QAH state, as shown in Figs. 1(c)–1(f), where the two-dimensional (2D) Ising exponents $\beta = 1/8$ and $\nu = 1$ for the scaling form $S(T, L)L^{2\beta/\nu} = f[(T - T_c)L^{1/\nu}]$, with f being the scaling function, are used. The obtained T_c reduces with increasing u_0, as shown in Fig. 1(a), and it can be extrapolated that, when $u_0 \approx 90$ meV, T_c is zero within our resolution as indicated by the dashed fitting line with an error of 5 meV.

Such vanishing of the QAH phase as a function of u_0 is consistent with the evolution of the quasiparticle gap of Γ, Δ_Γ, with different system sizes (N_k) at the temperature 3 meV, as shown in Fig. 2(a). The counterparts from ED also yield the same tendency, as shown in Fig. 11. The values of Δ_Γ are obtained from fitting imaginary time (τ) Green's functions (GFs) to a range with linear τ dependence of logarithmic GFs, see Figs. 9 and 10 in the Appendix. As a system should be gapless if there is at least one kind of gapless quasiparticles, therefore, the marginal and converged values of Δ_Γ of different system sizes indicate the system gapless when $u_0 > 0.8u_1$, as shown in Fig. 2(a) and Fig. 11, although quasiparticle gaps of other $\mathbf{k}$ points of mBZ remain significant even for large u_0, as shown in Fig. 10, suggesting an SM phase. In addition, as also depicted in Fig. 2(a), due to finite-size effect, the value of Δ_Γ with a small u_0 increases but converges as the system size enlarges. It is found as well that the values of T_c are much smaller than those of the quasiparticle gaps, due to particle-hole excitons with smaller energies above the QAH phase, which restore the broken time-reversal symmetry above T_c and has been evidenced in our previous works [38,63]. Moreover, the spectra (will be discussed below) of quasiparticles of the Dirac points in mBZ, K_1 and K_2 (see Fig. 7 for their positions), from the 6×6 system are always and well gapped through

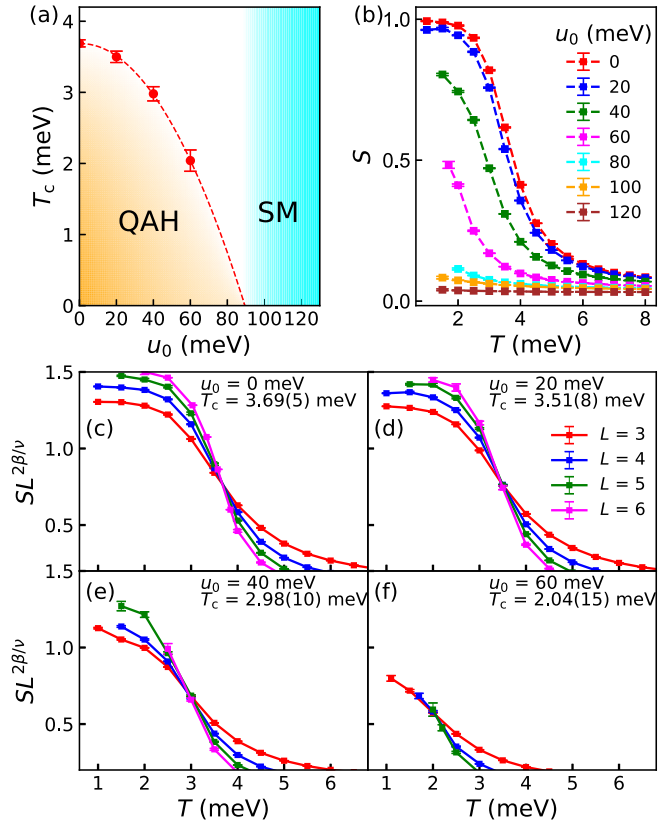

FIG. 1. QAH state to heavy-fermion semimetal transition away from chiral limit in the magic-angle TBG of $\nu = -3$. (a) The phase diagram, where T_c refers to the transition temperature of the QAH state, marking the time-reversal symmetry breaking and being determined by finite-size scaling crossings in (c)–(f), and the dased line is a fit to the data. (b) Chern number polarization, S, obtained from the $L = 4$ system, where the simulation T for each u_0 reaches as low temperature as possible. (c)–(f) Finite-size effect crossings with 2D Ising exponents to derive T_c.

the u_0 range investigated, as shown in Figs. 3(b)–3(d), which thus prove that the Dirac points do not play key roles in the transition towards the SM phase.

The charge compressibility, $\kappa = d\langle N \rangle / d\mu / n_0 / N_k = \beta(\langle N^2 \rangle - \langle N \rangle^2)/n_0/N_k$, where $N = \sum_m N_m$ and n_0 is the particle density, is also calculated to to evidence the transition from the QAH state to the SM state, whose values are shown in Fig. 2(b). The vanishing of κ indicates the state incompressible and insulating, and compressibly conducting otherwise. Therefore, a small u_0 yields an insulating ground state, which is the QAH phase, while a large u_0 leads to a conducting ground state, corresponding to the SM phase. Such that the Chern-number polarization, the quasiparticle gap, and the charge compressibility yield the same physics.

To further reveal the evolution from the QAH phase to the SM phase with increasing u_0, we derive the quasiparticle spectra, $A(\mathbf{k}, \omega)$, and the corresponding local density of state, $LDOS = \sum_\mathbf{k} A(\mathbf{k}, \omega)/N_\mathbf{k}$, from the stochastic analytic continuation scheme [64,65], the results of $L = 6$ system at $T = 3$ meV of which are shown in Fig. 3. As is consistent to T_c of the QAH phase at a specific u_0, $A(\mathbf{k}, \omega)$ is gapped for all $\mathbf{k}$ points when T is below T_c as shown in Fig. 3(b),

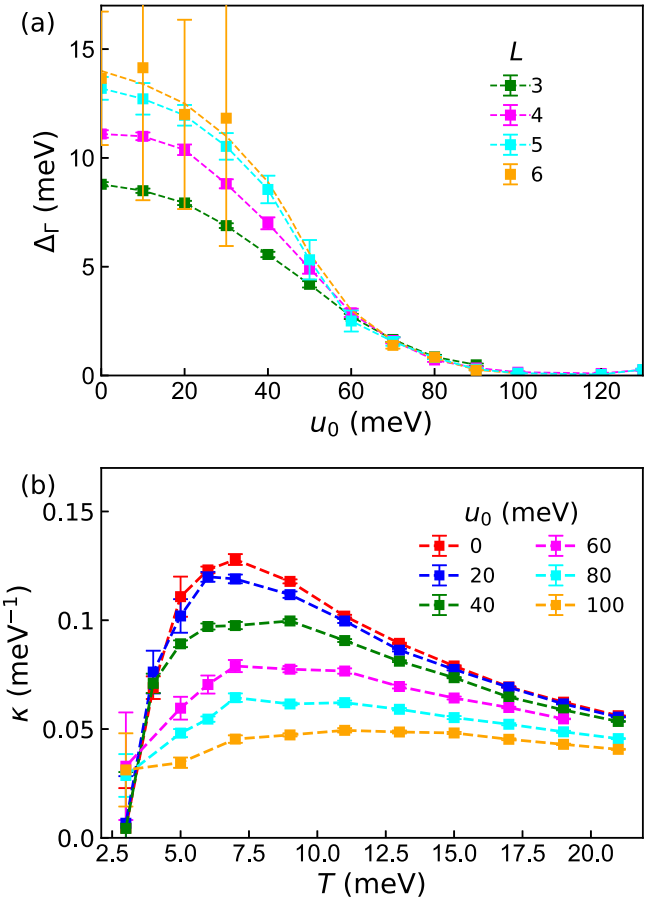

FIG. 2. Quasiparticle gap of Γ, Δ_Γ, and charge compressibility, κ, as functions of u_0 or T. (a) The simulation temperature is 3 meV considering the sign problem and the consistency to those of ED. (b) The system size is $L = 3$.

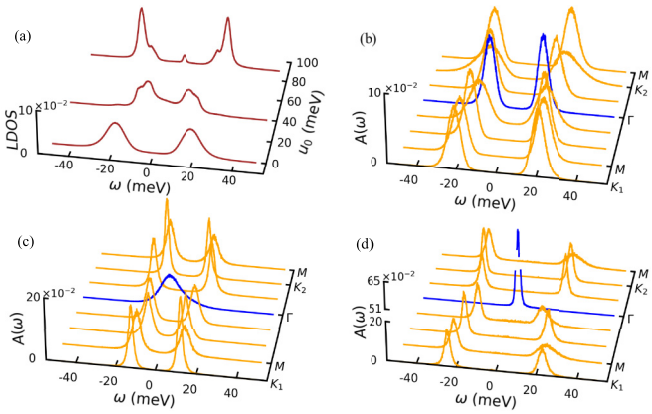

FIG. 3. LDOS and quasiparticle spectra with $L = 6$ and $T = 3$ meV. (a) Normalized local density of states (LDOS) versus energy ω and u_0. (b), (c), and (d) Single-particle spectra $A(\mathbf{k}, \omega)$ along a high-symmetry path when $u_0 = 0$, $u_0 = 40$ meV, and $u_0 = 90$ meV, respectively, where the blue lines denote the spectra of Γ, while the orange lines are $A(\mathbf{k}, \omega)$ of other momentum points. Please note that the vertical axis in (d) is broken, due to the sharp peak of Γ, to make the drawing compact. Mind that $T = 3$ meV is below T_c when $u_0 = 0$ but above it when $u_0 = 40$ meV.

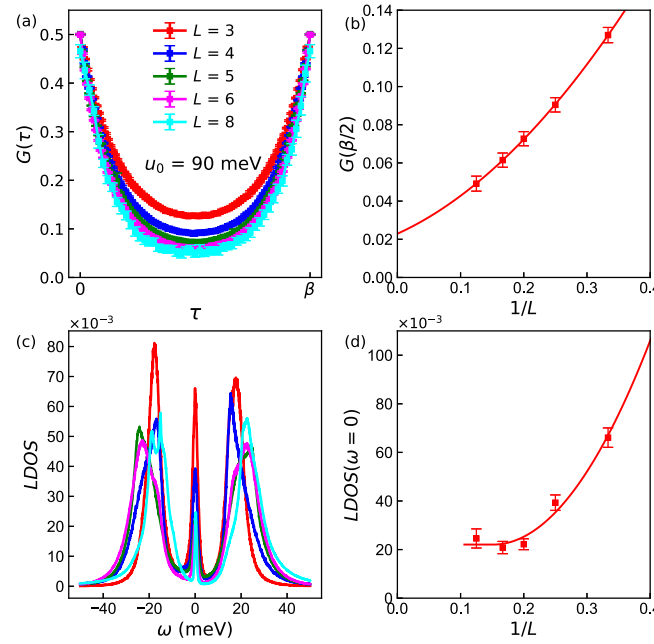

FIG. 4. (a) The decaying of average Green's function and the (c) reducing of the peak at Fermi level of LDOS with the system size up to $L = 8$ when $u_0 = 90$ meV. The extrapolations of $G(\beta/2)$ and the intensity of the peak of LDOS at Fermi level to larger sizes are shown in (b) and (d), respectively, where the fitting is quadratic due to that it is versus $1/L$, except the horizontal part in (d).

and gapless around Γ when T is slightly above T_c as shown in Fig. 3(c), suggesting the state above QAH a semimetal and the quasiparticles high-energy excitons. Therefore, T_cs set the phases boundary between QAH state and SM, indicating again the ground state of magic-angle TBG is semimetallic when $u_0 > 0.8u_1$, as being further evidenced by Fig. 3(d), which is consistent to the experimentally found SM phases [43–45]. The gap of $A(\Gamma, \omega)$ is the least and gradually decreases with growing u_0 [Figs. 3(b)–3(d)], where two peaks gradually merge into a single one. The gap totally closes when $u_0 = 90$ meV [Fig. 3(d)]. The LDOS remains gapped except a peak around Fermi level arises as u_0 increases [Fig. 3(a)]. This peak comes from the closing of Δ_Γ, as shown in Figs. 3(c) and 3(d), while the spectra of other quasiparticles remain well gapped.

Average Green's function summing over $\mathbf{k}$ points and LDOS with different linear sizes are demonstrated in Fig. 4, where $u_0 = 90$ meV. The convergence of decaying of $G(\tau)$ can be seen, and $G(\beta/2)$ reduces probably to a minimum but finite value at the large L limit, as shown in Figs. 4(a) and 4(b), respectively, suggesting that there are finite electrons at the Fermi level. Meanwhile, the peak of LDOS at Fermi level decreases probably to a minimum but finite value as the system size is larger than 6, as depicted in Fig. 4(d). The probable nonzero extrapolations suggest quadratic band touching of the semimetallic phase of the magic-angle TBG when $u_0 = 90$ meV. However, a linear fit extrapolating to 0, indicating degenerate Dirac cone touching, cannot be totally ruled out in both Figs. 4(b) and 4(d). To further verify that the probable semimetallic state is of quadratic band touching, here

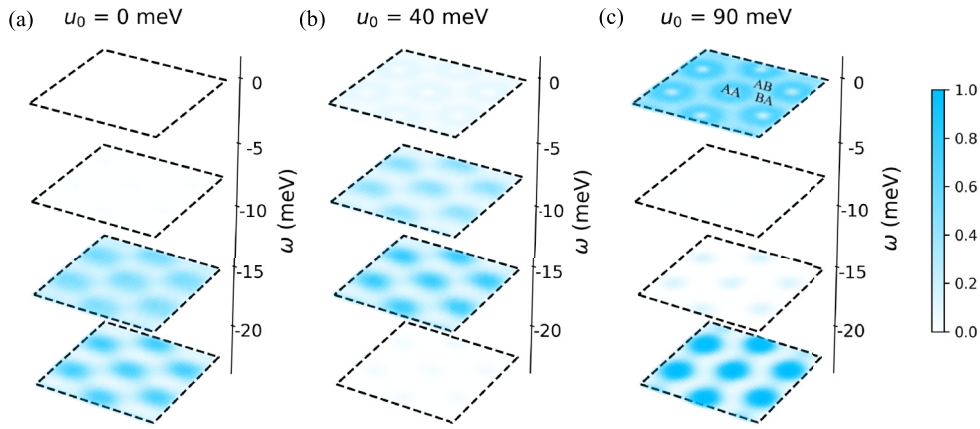

FIG. 5. Real-space spectra $A(r, \omega)$ at various u_0 and ω when $T = 3$ meV. Here u_0 equals to (a) 0 meV, (b) 40 meV, and (c) 90 meV, respectively, while ω is chosed to be 0, 7.5, 15, and 22.5 meV in each figure. The intensity of blue stands for the value of $A(r, \omega)$, with a color bar locating at the right of (c). Positions of AA, AB, and BA stacking areas are labeled in (c).

we check if the C_3 rotation symmetry is broken by scrutinizing the correlation of a nematic order parameter, which is defined as $\mathcal{N} = \frac{1}{N_k}\sum_k c^\dagger_{\mathbf{k},+}c_{\mathbf{k},-}$. The correlation of $\mathcal{N}$, $S_\mathcal{N} = \langle \mathcal{N}^\dagger \mathcal{N}\rangle$, is calculated and illustrated in Fig. 12, as the system is in the SM phase. Since the value of $S_\mathcal{N}$ extrapolates to zero towards the thermodynamic limit, the C_3 rotation symmetry is probably not broken. Therefore, our found SM phase is probably not nematic, enhancing the probability of the SM state being a quadratic band touching semimetal.

As degenerate Dirac cone touching cannot be ruled out, we argue that it is less probable in our case. Based on the Nielsen-Ninomiya theorem of fermion doubling [66], Dirac cones shall appear in pairs. The only way of obeying the fermion doubling theorem is to have two degenerate Dirac cones at Γ. However, considering that we only have one valley/spin degree of freedom (no symmetry to enforce twofold degeneracy), there is no obvious reason why the system would stabilize such a twofold degenerate energy spectrum. Nevertheless, it should be emphasized that this is not impossible, and it would imply that this semimetal phase is highly unconventional. Aside from the unconventional pathway towards Dirac semimetal, there is another less exotic possibility producing Dirac points: nematic Dirac semimetal. The system has a pair of Dirac points near Γ, one at a momentum point $\mathbf{q}$ and the other at $-\mathbf{q}$. However, such a scenario requires the breaking of rotational symmetry, which is probably preserved in our case, as indicated by $S_\mathcal{N}$. For quadratic band touching, as there is no constraint of doubling theorem, it is allowed to have a single quadratic band crossing at Γ.

The closing of the quasiparticle gap of Γ is consistent with the recently proposed heavy-fermion picture of magic-angle TBG [32,50–56]. In the heavy-fermion representations, the flat bands are mostly composed of localized electrons, except for the tiny vicinity of Γ, which is mainly contributed by delocalized electronic states. In the flat-band limit, strong interactions between localized electrons ought to induce energy gaps in the quasiparticle spectra. However, these interaction-induced gaps are expected to be much smaller in the narrow surrounding of Γ, since the fermion states there are delocalized with weaker interaction, and it is indeed so at chiral limit and when $u_0 = 40$ meV, as shown in Figs. 3(b) and 3(c). Moreover, the interactions among fermions around Γ can be further weaker as the system deviates from chiral limit, and the corresponding quasiparticle gaps decline and eventually close when u_0 goes beyond a threshold value ($u_0 \approx 0.8u_1$ judged from T_c), as also illustrated by Fig. 3(d).

To further scrutinize the heavy-fermion features of the SM phase, here we directly probe the localized and delocalized electron states via real-space spectra by projecting $A(\mathbf{k}, \omega)$ of the $L = 6$ system at $T = 3$ meV with the real-space wave function $\psi_\mathbf{k}(\mathbf{r}, X)$ of H_0, $A(r, \omega) = \sum_{\mathbf{k},X} \psi^\dagger_\mathbf{k}(\mathbf{r}, X)A(\mathbf{k}, \omega)\psi_\mathbf{k}(\mathbf{r}, X)$, as a function of u_0 and shown in Fig. 5. It can be clearly seen that the density of low-energy electrons [$\omega = 0$ meV, first row of Figs. 5(a)–5(c)] increases in AB/BA stacking regions (or is lifted as the maximum values are around AA stacking center, where, however, the minimum values locate), marking the emergence of the SM state. Meanwhile, the localized electrons [$\omega =$ 15, 22.5 meV, bottom two rows of Figs. 5(a)–5(c)] always and further concentrate at AA centers as u_0 grows, which is consistent with the heavy-fermion picture [50,51] and experiments [8,9]. Furthermore, the density of electrons with intermediate energy [$\omega = 7.5$ meV, second row in Fig. 5(c)] manifests a minimum value, separating the itinerant and localized electrons when $u_0 = 90$ meV. These observations suggest that the realistic (when $u_0 \approx 0.8u_1$) magic-angle TBG of $\nu = -3$ can be preliminary viewed as a heavy-fermion system. Besides, the itinerant electrons of $A(r, \omega = 0)$ in Fig. 5(c) come from $A(\Gamma, \omega = 0)$ in Fig. 3(d).

IV. DISCUSSIONS

In this study, an evolution from the Chern insulator to a heavy-fermion semimetal probably preserving C_3 symmetry is found for $\nu = -3$ filling magic-angle TBG by increasing AA hopping strength, u_0, which can be experimentally altered. The ground-state phase transition happens at $u_0 \approx 0.8u_1$ or

90 meV, where the Chern-number polarization and the quasiparticle gap of Γ vanish, the system becomes compressible, and a peak in LDOS at Fermi level emerges due to the gap's closing. The intensity of this peak rises as u_0 increases for a specific system size, but reduces probably to a minimum but finite value as L enlarges for a specific u_0, which manifests a semimetal state as the gaps of other momenta remain significant. The momentum and real-space distributions of the localized electrons are well separated from those of itinerant electrons, which are of the Γ point. The nature of the found semimetal state implies that the magic-angle TBG can be preliminarily, based on the numerics here, treated as a heavy-fermion system when $\nu = -3$. Our findings shed new light on the correlated nature of TBG and provide critical information for understanding this fascinating system.

ACKNOWLEDGMENTS

We thank DongKeun Ki and Wang Yao for useful discussions. C.H., X.Z., G.P.P., and Z.Y.M. acknowledge the support from the Research Grants Council (RGC) of Hong Kong SAR of China (Projects No. 17302223, No. 17301721, No. AoE/P-701/20, No. 17309822, and No. C7037-22GF), the ANR/RGC Joint Research Scheme sponsored by RGC of Hong Kong and French National Research Agency (Project No. A_HKU703/22), the Strategic Priority Research Program of Chinese Academy of Sciences (Grant No. XDB33000000), and K. C. Wong Education Foundation (Grant No. GJTD-2020-01). We thank the HPC2021 system of Information Technology Services and the Blackbody HPC system at the Department of Physics, of the University of Hong Kong, and Beijing PARATERA Tech Co., Ltd. (https://cloud.paratera.com) for providing computational resources that have contributed to the research results in this paper.

APPENDIX A: MOMENTUM-SPACE DETERMINANT QMC METHOD

Due to the flatness of the lowest-energy bands, as shown in Fig. 8, H_0 is ignored in our simulations. The partition function thus reads $Z = \mathrm{Tr}(\mathrm{e}^{-\beta H_\mathrm{I}})$, where $\beta = 1/k_\mathrm{B}T$ and T is the temperature. Z can be Trotter decoupled after splitting inverse temperature into N_τ pieces, $\beta = \triangle\tau N_\tau$, with an error of order $\triangle\tau^2$. That is

$$\begin{aligned} Z &= \mathrm{Tr}(\mathrm{e}^{-\beta H_\mathrm{I}}) \\ &= \mathrm{Tr}((\mathrm{e}^{-\triangle\tau H_\mathrm{I}})^{N_\tau}) \\ &= \mathrm{Tr}\left(\prod_{\tau=\triangle\tau}^{\beta} \mathrm{e}^{-\triangle\tau H_\mathrm{I}}\right) + \mathcal{O}(\triangle\tau^2). \end{aligned} \tag{A1}$$

Denoting $\mathbf{Q} = \mathbf{q} + \mathbf{G}$, H_I can be rewritten as

$$\begin{aligned} H_\mathrm{I} &= \sum_{|\mathbf{Q}|\neq 0} \frac{1}{2\Omega} V(\mathbf{Q}) \delta\rho_{\mathbf{Q}} \delta\rho_{-\mathbf{Q}} \\ &= \sum_{\mathcal{Q}} \frac{1}{2\Omega} V(\mathcal{Q}) (\delta\rho_{\mathcal{Q}} \delta\rho_{-\mathcal{Q}} + \delta\rho_{-\mathcal{Q}} \delta\rho_{\mathcal{Q}}) \\ &= \sum_{\mathcal{Q}} \frac{1}{4\Omega} V(\mathcal{Q}) ((\delta\rho_{-\mathcal{Q}} + \delta\rho_{\mathcal{Q}})^2 - (\delta\rho_{-\mathcal{Q}} - \delta\rho_{\mathcal{Q}})^2), \end{aligned} \tag{A2}$$

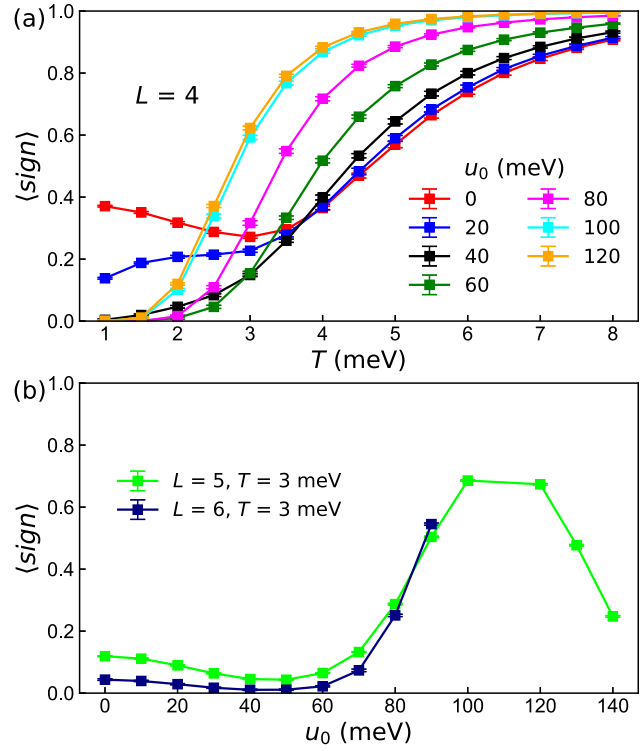

FIG. 6. ⟨sign⟩ of magic-angle TBG with $\nu = -3$, when (a) $L = 4$ varying T and u_0, and (b) $L = 5, 6$ and $T = 3$ meV varying u_0. ⟨sign⟩ reaches 0 when $u_0 \geqslant 40$ meV as $T = 1$ meV in (a), while ⟨sign⟩ of $L = 6$ reaches 0.01 when $u_0 = 40$ meV in (b).

where $\mathcal{Q}$ is the half of $|\mathbf{Q}| \neq 0$ [35]. Thus, $\mathrm{e}^{-\triangle\tau H_\mathrm{I}}$ can be further decoupled to an auxiliary field by the Hubbard-Stratonovich transformation, with an error of

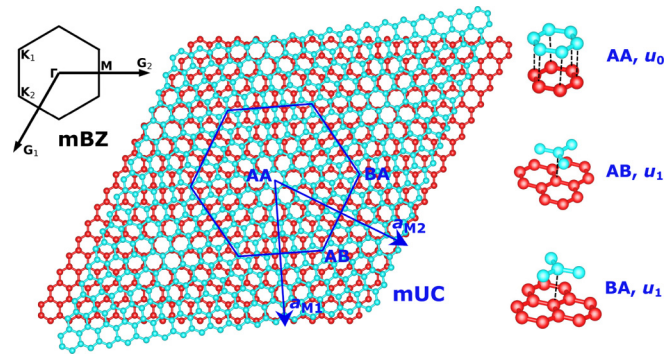

FIG. 7. Moiré unit cell (blue hexagon) and its Brillouin zone (black hexagon), as well as three kinds of stackings and hoppings (AA, AB, and BA) of TBG. u_0 and u_1 are hopping strengths of AA- and AB/BA-stacking areas, respectively. The top (bottom) layer of TBG are denoted by cyan (red) color. $\{\mathbf{a}_{\mathrm{M}1}, \mathbf{a}_{\mathrm{M}2}\}$ and $\{\mathbf{G}_1, \mathbf{G}_2\}$ are the lattice vectors of mUC and mBZ, respectively. Γ is the origin of mBZ, and $\mathbf{K}_1$ and $\mathbf{K}_2$ are the two Dirac points of the same vellay and different layers (1, 2). The twisted angle θ in this schematic is 10°, while that of the case we investigate in the main text is 1.08°.

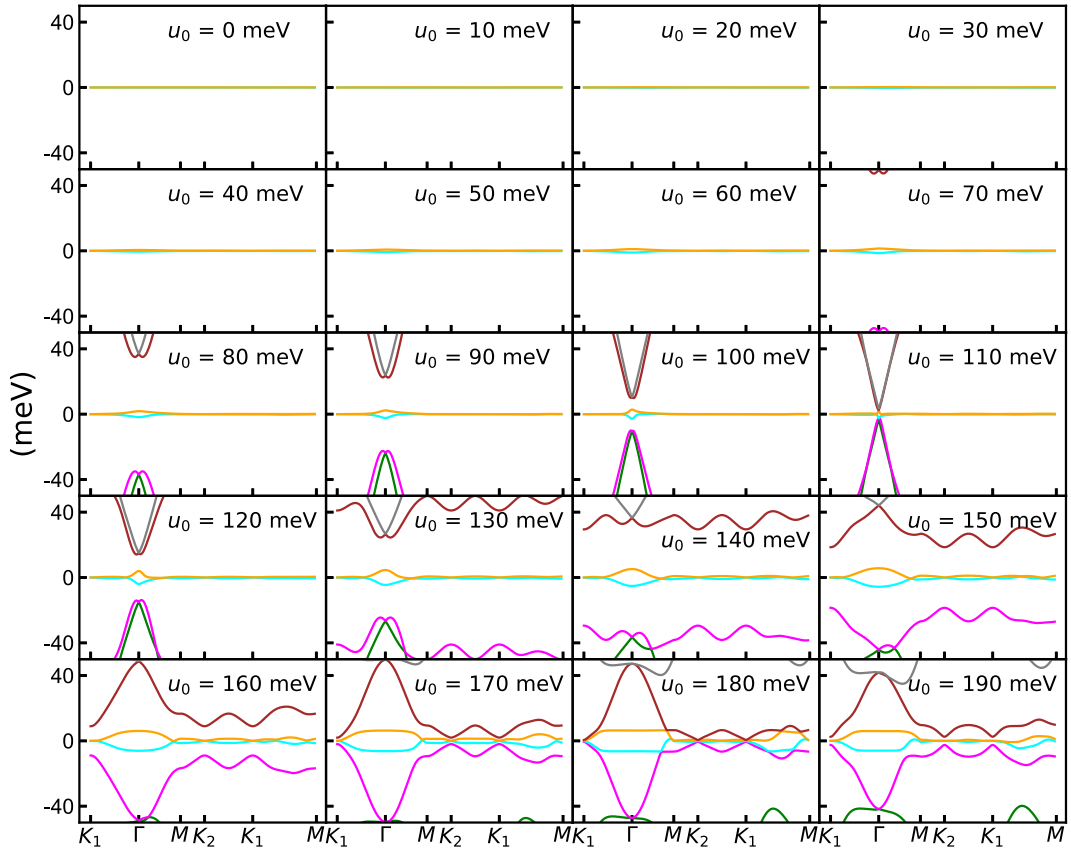

FIG. 8. Single-particle dispersions of H_0 at the first magic angle and along a high-symmetry line. The remote bands are beyond the scale when $u_0 < 70$ meV, and approaches the flat bands around Γ point as u_0 further increases. Note that the lowest remote bands touch the flat bands at Γ point only when $u_0 = 110$ meV ($u_0 = u_1$). The band width of the flat bands enlarge as u_0 increases, but remains a quite small value (less than 5 meV when $u_0 = 90$ meV).

order $\triangle\tau^4$, as

$$e^{-\triangle\tau H_1} = \prod_{\mathcal{Q}} \frac{1}{16} \sum_{l_{1\mathcal{Q}}, l_{2\mathcal{Q}}} \gamma(l_{1\mathcal{Q}})\gamma(l_{2\mathcal{Q}}) \times e^{i\sqrt{\alpha}\eta(l_{1\mathcal{Q}})(\delta\rho_{-\mathcal{Q}}+\delta\rho_{\mathcal{Q}})} e^{\sqrt{\alpha}\eta(l_{2\mathcal{Q}})(\delta\rho_{-\mathcal{Q}}-\delta\rho_{\mathcal{Q}})} + \mathcal{O}(\triangle\tau^4), \tag{A3}$$

where $l = \pm 1, \pm 2$, is the auxilariy field, and $\gamma(\pm 1) = 1 + \sqrt{6}/3$, $\gamma(\pm 2) = 1 - \sqrt{6}/3$, $\eta(\pm 1) = \pm\sqrt{6 - 2\sqrt{6}}$, and $\eta(\pm 2) = \pm\sqrt{6 + 2\sqrt{6}}$. $\alpha = \triangle\tau V(\mathcal{Q})/4\Omega$.

The partition function can be finally written as $Z = \sum_{\{l_{\tau 1\mathcal{Q}}, l_{\tau 2\mathcal{Q}}\}} \mathrm{Tr} U_C$, with

$$U_C = \prod_{\tau=\triangle\tau}^{\beta} \prod_{\mathcal{Q}} \frac{1}{16} \gamma(l_{\tau 1\mathcal{Q}})\gamma(l_{\tau 2\mathcal{Q}}) \times e^{i\sqrt{\alpha}\eta(l_{\tau 1\mathcal{Q}})(\delta\rho_{-\mathcal{Q}}+\delta\rho_{\mathcal{Q}})} e^{\sqrt{\alpha}\eta(l_{\tau 2\mathcal{Q}})(\delta\rho_{-\mathcal{Q}}-\delta\rho_{\mathcal{Q}})}, \tag{A4}$$

a configuration of $\{l_{\tau 1\mathcal{Q}}, l_{\tau 2\mathcal{Q}}\}$ labeled by C. Physical quantities, O, can thus be obtained by sampling the auxiliary field, as

$$\begin{aligned} \langle O \rangle &= \frac{\mathrm{Tr}(e^{-\beta H_1} O)}{Z} \\ &= \sum_C \frac{\mathrm{Tr}(U_C O)}{Z} \\ &= \sum_C \frac{\mathrm{Tr}(U_C)}{Z} \frac{\mathrm{Tr}(U_C O)}{\mathrm{Tr}(U_C)}, \end{aligned} \tag{A5}$$

with $\mathrm{Tr}(U_C)/Z$ or $\mathrm{Tr}(U_C)$ the sampling weight and denoted as P_C.

However, P_C of the magic-angle TBG with $\nu = -3$ is not constantly positive, or sign problematic, as shown in Fig. 6. Nevertheless, the symmetries of TBG make P_C real [35] and the average of its sign, $\langle \mathrm{sign} \rangle = \sum_C \mathrm{sgn}(P_C)$, is always positive and ranges from 0–1. Here 1 means no sign problem while 0 means the simulation is valueless. It is quite intuitive how to avoid negative weight. Denoting $O_C = \mathrm{Tr}(U_C O)/\mathrm{Tr}(U_C)$, $\langle O \rangle$ can be rewritten as

$$\begin{aligned} \langle O \rangle &= \frac{\sum_C O_C P_C}{\sum_C P_C} \\ &= \frac{\sum_C O_C \mathrm{sgn}(P_C)|P_C| / \sum_C |P_C|}{\sum_C \mathrm{sgn}(P_C)|P_C| / \sum_C |P_C|}. \end{aligned} \tag{A6}$$

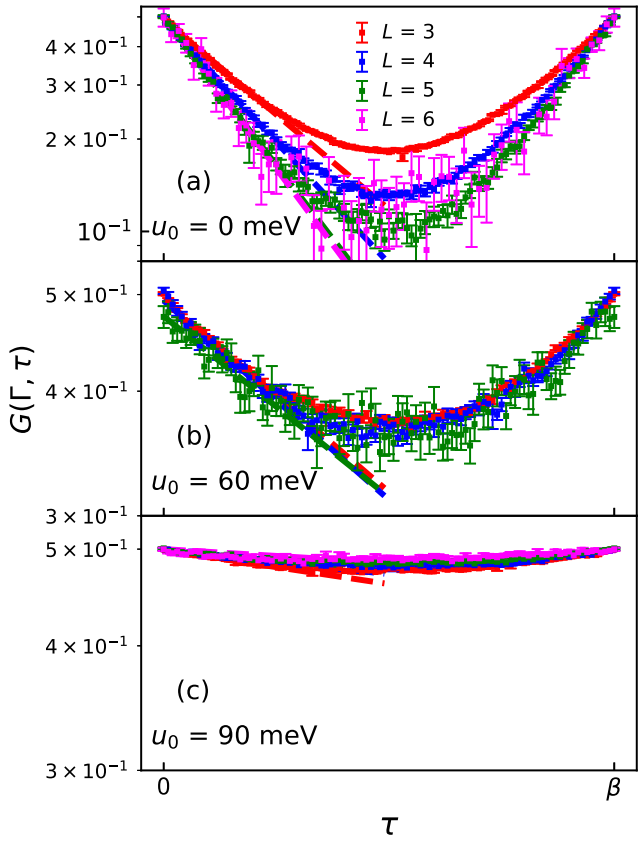

FIG. 9. Decaying of imaginary time Green's function of Γ point with $L = 3, 4, 5, 6$, when (a) $u_0 = 0$ meV, (b) $u_0 = 60$ meV, and (c) $u_0 = 90$ meV, where the log scale is used. Mind that the vertical scales of (b) and (c) is different from that of (a). The fitting dashed lines are also shown in each panel, the slopes of which give the quasiparticle gaps in Figs. 2(a) and 10.

Thus, the numerator and the denominator can be sampling separately by $|P_C|/\sum_C |P_C|$, with $O_C \mathrm{sgn}(P_C)$ and $\mathrm{sgn}(P_C)$ being the measured quantities, and $\langle O \rangle$ can be further obtained.

Our stable and reproducible results show that a QMC simulation can still be efficiently and reliably done when $\langle \mathrm{sign} \rangle > 0.01$ with reasonable computing resources. In the obtaining of reliable imaginary time Green's function, the simulation temperature is set to be $T = 3$ meV considering the $\langle \mathrm{sign} \rangle$ of the $L = 6$ system, while the T can be lowered when measuring Chern-number polarization. With the reliable imaginary time Green's function, we further employ the stochastic analytic continuation (SAC) [36,38,67–70] method to extract the real frequency spectra.

APPENDIX B: MOIRÉ SUPERLATTICE AND SINGLE-PARTICLE DISPERSIONS

The real-space moiré superlattice generated by TBG is shown in Fig. 7, where a mUC and its reciprocal first Brillouin zone (mBZ) are drawn. The module of the lattice vectors of mBZ is $|\mathbf{G}_1|$, $|\mathbf{G}_2| = 8\pi \sin(\theta/2)/(3a)$. $\mathbf{K}_1^\eta$ and $\mathbf{K}_2^\eta$ are Dirac points from the top (1) and bottom (2) layers, respectively. Schematics of hopping patterns are also shown in the right panel of Fig. 7. In this work, we consider the system with the first magic angle ($\theta = 1.08^\circ$).

From this moiré superlattice, a momentum space single-particle Hamiltonian, H_0, considering intralayer hopping and interlayer hopping, can be constructed, as described in the main text. The dispersions of H_0 at the magic angle with different u_0 are shown in Fig. 8, where two low-energy bands are quite flat and isolated from remote bands when $u_0 \leqslant 90$ meV. It implies that the low-energy physics can be well captured by these two bands. The projection of H onto flat bands, as depicted in the main text, makes the description of H easier since only two bands are considered. However, we suppose that the

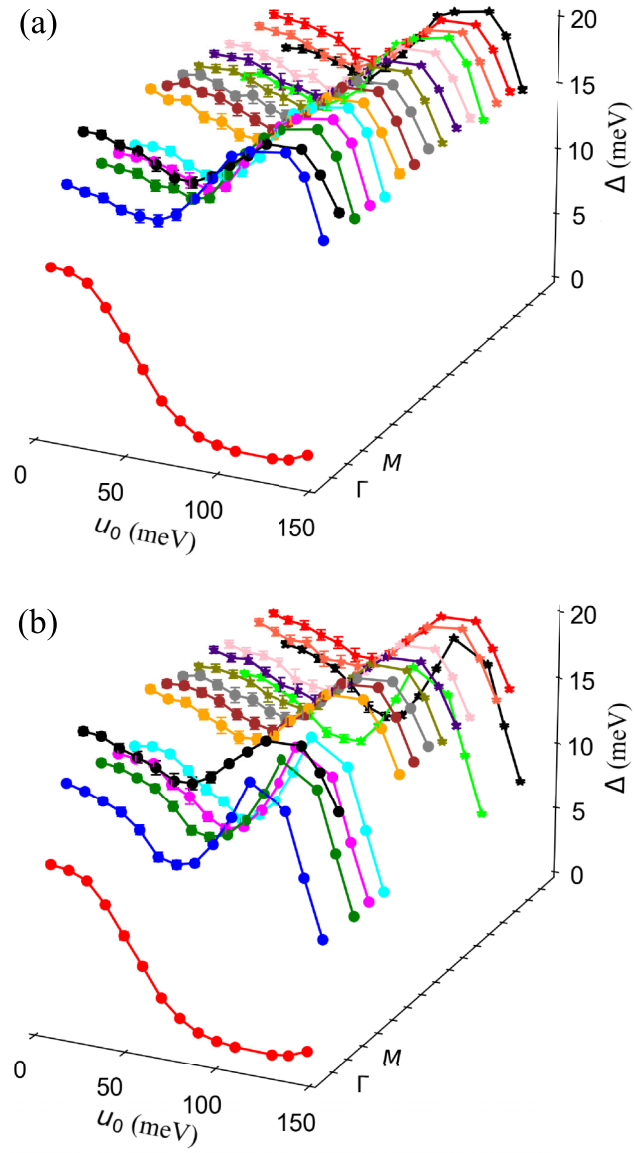

FIG. 10. Quasiparticle gaps of two bands, ±, (a) and (b), of **k** points in mBZ with $L = 4$ and varying u_0. Here Γ and M refer to the red circle line and the black circle line, respectively, and the rest circle lines or star lines are those of the rest momentum points. Error bars of many data points are smaller than corresponding markers' sizes. Note that the gaps of − band remain quite large values (>8 meV) when $u_0 = 150$ meV, as shown in (b).

projections when $u_0 = 110$ (meV) and $u_0 > 160$ (meV) fail as remote bands are too close to flat bands.

APPENDIX C: CALCULATION OF CHERN-NUMBER POLARIZATION

A perturbation term, which reads

$$\delta H = \begin{pmatrix} 0 & 0 \\ 0 & \delta\sigma_z \end{pmatrix}, \tag{C1}$$

with $\delta = 1\,\text{meV}$ and σ_z being the third Pauli matrix, is added to the bottom layer of H_0 to break inversion and an isolated Chern bands basis $|\psi\rangle$ is obtained. This perturbation term breaks $C_{2z}\mathcal{T}$ but $\mathcal{T}$, which means the spontaneous time-reversal symmetry breaking of the TBG system is still allowed. Denoting the original basis as $|\phi\rangle$, the imaginary-time Green's function in the isolated Chern bands basis can thus be related to the original basis, by $\langle\psi|G(\mathbf{k})|\psi'\rangle = \sum_{\phi,\phi'}\langle\psi|\phi\rangle\langle\phi|G(\mathbf{k})|\phi'\rangle\langle\phi'|\psi'\rangle$. Thus, the correlation function of the QAH order, or Chern-number polarization, can be calculated in the isolated Chern band basis. As this perturbation term resembles an h-BN potential, therefore the strength, δ, which can be as low as 0.3 meV, is chosen to be 1 meV to minimize the relevance. This perturbation term is only added when calculating Chern-number polarization.

APPENDIX D: IMAGINARY TIME GREEN'S FUNCTION AND DERIVED GAPS

The decaying of $G(\Gamma, \tau)$ is depicted in Fig. 9, where the convergence of decaying can be seen with increasing L. The minimum single-particle gap of each momentum can be obtained by fitting $G(\tau) = \exp(-\Delta\tau)/2 + \exp[-\Delta(\beta - \tau)]/2$ to the data in a range with linear τ dependence of logarithmic GFs as shown in Fig. 9, and the obtained gaps are demonstrated in Fig. 2(a) and Fig. 10, where those of other $\mathbf{k}$ points are also shown.

The gaps of $L = 3$ from ED, considering the computational complexity, is calculated as well and shown in Fig. 11 (green squares), where counterparts from QMC (red squares), with the simulation temperature being 3 meV, are also shown. As the result from ED is of ground state, gaps from QMC at 3 meV are slightly lower than those from ED, and the lowering of simulation T can reduce the deviation. Besides, the same tendency is obtained that the gap closes at $u_0 \approx 0.8u_1$. In addition, the detail of implementation of ED is depicted in Appendix F.

APPENDIX E: C_3 ROTATION SYMMETRY OF THE SEMIMETALLIC PHASE

The correlation of the nematic order, $\mathcal{N}$, as a function of reversed linear size, $1/L$, with $u_0 = 90\,\text{meV}$ is shown in Fig. 12. As there might be some correlation in a small system, there is none in the thermodynamic limit, suggesting the absence of this nematic order and the presence of C_3 rotation symmetry.

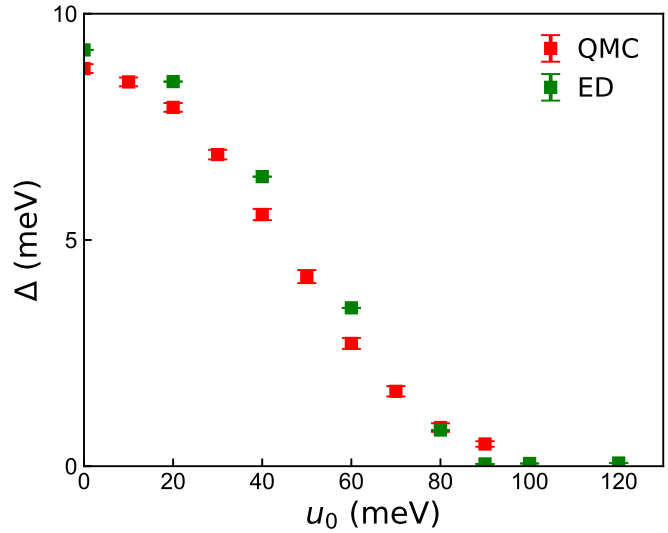

FIG. 11. Quasiparticle gaps of Γ from ED (green squares) when $L = 3$ compared with counterparts from QMC (red squares) with $T = 3\,\text{meV}$.

APPENDIX F: IMPLEMENTATION OF THE EXACT DIAGONALIZATION

Exact diagonalization (ED) is implemented to obtain the charge gap of the system in comparison to those from QMC. For $L \times L$ ($\equiv N_k$) systems with the two nearly flat bands taken into account, there are $2L^2$ single-particle states in total, which are labeled by momentum and band index. Here we use an integer $i \in [0, 2L^2 - 1]$ to label each single-particle state, $d_i^\dagger \equiv d_{\mathbf{k}m}^\dagger$, whose momentum $\mathbf{k}$ and band index m are determined by i. The Hamiltonian in Eq. (6) can be rewritten in the following form by moving all electron creation operator to the left:

$$H = \sum_{i,i',j',j} V_2(i,i',j',j) d_i^\dagger d_{i'}^\dagger d_{j'} d_j + \sum_{i,j} V_1(i,j) d_i^\dagger d_j + V_0. \tag{F1}$$

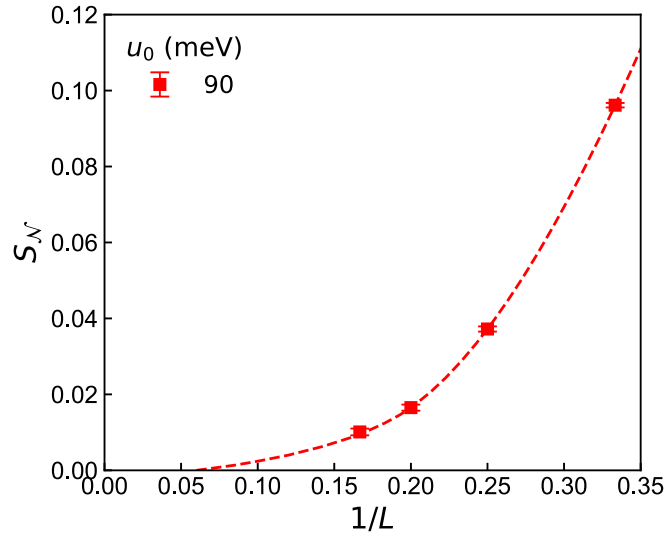

FIG. 12. Correlation, $S_\mathcal{N}$, of the nematic order parameter, $\mathcal{N}$, as a function of reversed linear size, $1/L$.

The matrix element between arbitrary many-body states can be obtained from Eq. (F1). Let $|\psi\rangle$ be a simple direct product state $|\psi\rangle = C^\dagger_{i_{N-1}} ... C^\dagger_{i_0}|0\rangle$ whose creation operators are ordered by $i_{N-1} > \cdots > i_1 > i_0$. Then $|\psi\rangle$ can also be represented by a string of bits with length $2L^2$ such as $|1101001...\rangle$. The Hamiltonian can be written in the basis made of these distinct direct product states. For a given product state $|\psi\rangle$, if there is another product state $|\psi'\rangle$ such that $\langle\psi'|H|\psi\rangle \neq 0$, then either of the two situations occurs: (i) there exist distinct numbers $i \neq i'$ such that $|\psi'_1\rangle \propto d^\dagger_{i'} d_i|\psi\rangle$; (ii) there exist distinct numbers i, j, i', j' with $i > j, i' > j'$ such that $|\psi'_2\rangle \propto d^\dagger_{j'} d^\dagger_{i'} d_i d_j|\psi\rangle$. Then, according to Eq. (F1), we have

$$\langle\psi'_2|H|\psi\rangle = (-1)^{\mu(i,j)}(-1)^{\mu'(i',j')}[V_2(j', i', i, j) - V_2(j', i', j, i) - V_2(i', j', i, j) + V_2(i', j', j, i)]. \tag{F2}$$

Here $\mu(i, j)$ is the number of "1" between the ith and jth bits in the bit representation of $|\psi\rangle$. This sign factor comes from the Fermi anticommutation of creation operators. Similarly, for $|\psi'_1\rangle \propto d^\dagger_{i'} d_i|\psi\rangle$, we have

$$\langle\psi'_1|H|\psi\rangle = \sum_j (-1)^{\mu(i,j)}(-1)^{\mu'(i',j)}[V_2(j, i', i, j) - V_2(i', j, i, j) - V_2(j, i', j, i) + V_2(i', j, j, i)] + V_1(i', i). \tag{F3}$$

The diagonal matrix elements are

$$\langle\psi|H|\psi\rangle = V_0 + \sum_{i>j, \psi_i=\psi_j="1"} [V_2(j, i, i, j) - V_2(j, i, j, i) - V_2(i, j, i, j) + V_2(i, j, j, i)] + \sum_{i, \psi_i="1"} V_1(i, i). \tag{F4}$$

Then H can be diagonalized in the basis of $|\psi\rangle$ to obtain its eigenvalues.

[1] G. Trambly de Laissardière, D. Mayou, and L. Magaud, Localization of Dirac electrons in rotated graphene bilayers, Nano Lett. **10**, 804 (2010).

[2] G. Trambly de Laissardière, D. Mayou, and L. Magaud, Numerical studies of confined states in rotated bilayers of graphene, Phys. Rev. B **86**, 125413 (2012).

[3] R. Bistritzer and A. H. MacDonald, Moiré bands in twisted double-layer graphene, Proc. Natl. Acad. Sci. **108**, 12233 (2011).

[4] Y. Cao, V. Fatemi, A. Demir, S. Fang, S. L. Tomarken, J. Y. Luo, J. D. Sanchez-Yamagishi, K. Watanabe, T. Taniguchi, E. Kaxiras *et al.*, Correlated insulator behaviour at half-filling in magic-angle graphene superlattices, Nature (London) **556**, 80 (2018).

[5] Y. Cao, D. Rodan-Legrain, O. Rubies-Bigorda, J. M. Park, K. Watanabe, T. Taniguchi, and P. Jarillo-Herrero, Tunable correlated states and spin-polarized phases in twisted bilayer–bilayer graphene, Nature (London) **583**, 215 (2020).

[6] H. Polshyn, M. Yankowitz, S. Chen, Y. Zhang, K. Watanabe, T. Taniguchi, C. R. Dean, and A. F. Young, Large linear-in-temperature resistivity in twisted bilayer graphene, Nat. Phys. **15**, 1011 (2019).

[7] X. Liu, Z. Wang, K. Watanabe, T. Taniguchi, O. Vafek, and J. Li, Tuning electron correlation in magic-angle twisted bilayer graphene using coulomb screening, Science **371**, 1261 (2021).

[8] Y. Xie, B. Lian, B. Jäck, X. Liu, C.-L. Chiu, K. Watanabe, T. Taniguchi, B. A. Bernevig, and A. Yazdani, Spectroscopic signatures of many-body correlations in magic-angle twisted bilayer graphene, Nature (London) **572**, 101 (2019).

[9] Y. Choi, J. Kemmer, Y. Peng, A. Thomson, H. Arora, R. Polski, Y. Zhang, H. Ren, J. Alicea, G. Refael *et al.*, Electronic correlations in twisted bilayer graphene near the magic angle, Nat. Phys. **15**, 1174 (2019).

[10] K. P. Nuckolls, M. Oh, D. Wong, B. Lian, K. Watanabe, T. Taniguchi, B. A. Bernevig, and A. Yazdani, Strongly correlated Chern insulators in magic-angle twisted bilayer graphene, Nature (London) **588**, 610 (2020).

[11] Y. Saito, J. Ge, L. Rademaker, K. Watanabe, T. Taniguchi, D. A. Abanin, and A. F. Young, Hofstadter subband ferromagnetism and symmetry-broken Chern insulators in twisted bilayer graphene, Nat. Phys. **17**, 478 (2021).

[12] I. Das, X. Lu, J. Herzog-Arbeitman, Z.-D. Song, K. Watanabe, T. Taniguchi, B. A. Bernevig, and D. K. Efetov, Symmetry-broken Chern insulators and Rashba-like Landau-level crossings in magic-angle bilayer graphene, Nat. Phys. **17**, 710 (2021).

[13] S. Wu, Z. Zhang, K. Watanabe, T. Taniguchi, and E. Y. Andrei, Chern insulators, van Hove singularities and topological flat bands in magic-angle twisted bilayer graphene, Nat. Mater. **20**, 488 (2021).

[14] P. Potasz, M. Xie, and A. H. MacDonald, Exact diagonalization for magic-angle twisted bilayer graphene, Phys. Rev. Lett. **127**, 147203 (2021).

[15] A. Jaoui, I. Das, G. Di Battista, J. Díez-Mérida, X. Lu, K. Watanabe, T. Taniguchi, H. Ishizuka, L. Levitov, and D. K. Efetov, Quantum critical behaviour in magic-angle twisted bilayer graphene, Nat. Phys. **18**, 633 (2022).

[16] Y. Cao, V. Fatemi, S. Fang, K. Watanabe, T. Taniguchi, E. Kaxiras, and P. Jarillo-Herrero, Unconventional superconductivity in magic-angle graphene superlattices, Nature (London) **556**, 43 (2018).

[17] Y. Cao, D. Rodan-Legrain, J. M. Park, N. F. Yuan, K. Watanabe, T. Taniguchi, R. M. Fernandes, L. Fu, and P. Jarillo-Herrero, Nematicity and competing orders in superconducting magic-angle graphene, Science **372**, 264 (2021).

[18] M. Yankowitz, S. Chen, H. Polshyn, Y. Zhang, K. Watanabe, T. Taniguchi, D. Graf, A. F. Young, and C. R. Dean, Tuning superconductivity in twisted bilayer graphene, Science **363**, 1059 (2019).

[19] J. Diez-Merida, A. Díez-Carlón, S. Yang, Y.-M. Xie, X.-J. Gao, K. Watanabe, T. Taniguchi, X. Lu, K. T. Law, and D. K. Efetov, Magnetic Josephson junctions and superconducting diodes in magic angle twisted bilayer graphene, arXiv:2110.01067.

[20] G. Di Battista, P. Seifert, K. Watanabe, T. Taniguchi, K. C. Fong, A. Principi, and D. K. Efetov, Revealing the

thermal properties of superconducting magic-angle twisted bilayer graphene, Nano Lett. **22**, 6465 (2022).
[21] B. Lian, Z.-D. Song, N. Regnault, D. K. Efetov, A. Yazdani, and B. A. Bernevig, Twisted bilayer graphene. IV. Exact insulator ground states and phase diagram, Phys. Rev. B **103**, 205414 (2021).
[22] F. Xie, A. Cowsik, Z.-D. Song, B. Lian, B. A. Bernevig, and N. Regnault, Twisted bilayer graphene. VI. An exact diagonalization study at nonzero integer filling, Phys. Rev. B **103**, 205416 (2021).
[23] N. Bultinck, E. Khalaf, S. Liu, S. Chatterjee, A. Vishwanath, and M. P. Zaletel, Ground state and hidden symmetry of magic-angle graphene at even integer filling, Phys. Rev. X **10**, 031034 (2020).
[24] P. Wilhelm, T. C. Lang, and A. M. Läuchli, Interplay of fractional Chern insulator and charge density wave phases in twisted bilayer graphene, Phys. Rev. B **103**, 125406 (2021).
[25] M. Xie and A. H. MacDonald, Nature of the correlated insulator states in twisted bilayer graphene, Phys. Rev. Lett. **124**, 097601 (2020).
[26] Y. Zhang, K. Jiang, Z. Wang, and F. Zhang, Correlated insulating phases of twisted bilayer graphene at commensurate filling fractions: A Hartree-fock study, Phys. Rev. B **102**, 035136 (2020).
[27] J. Liu and X. Dai, Theories for the correlated insulating states and quantum anomalous Hall effect phenomena in twisted bilayer graphene, Phys. Rev. B **103**, 035427 (2021).
[28] K. Hejazi, X. Chen, and L. Balents, Hybrid Wannier Chern bands in magic angle twisted bilayer graphene and the quantized anomalous Hall effect, Phys. Rev. Res. **3**, 013242 (2021).
[29] F. Xie, J. Kang, B. A. Bernevig, O. Vafek, and N. Regnault, Phase diagram of twisted bilayer graphene at filling factor $\nu = \pm 3$, Phys. Rev. B **107**, 075156 (2023).
[30] X. Lin and J. Ni, Symmetry breaking in the double moiré superlattices of relaxed twisted bilayer graphene on hexagonal boron nitride, Phys. Rev. B **102**, 035441 (2020).
[31] Y. H. Kwan, G. Wagner, N. Chakraborty, S. H. Simon, and S. A. Parameswaran, Domain wall competition in the Chern insulating regime of twisted bilayer graphene, Phys. Rev. B **104**, 115404 (2021).
[32] A. Datta, M. J. Calderón, A. Camjayi, and E. Bascones, Heavy quasiparticles and cascades without symmetry breaking in twisted bilayer graphene, Nat. Commun. **14**, 5036 (2023).
[33] J. Kang and O. Vafek, Non-abelian Dirac node braiding and near-degeneracy of correlated phases at odd integer filling in magic-angle twisted bilayer graphene, Phys. Rev. B **102**, 035161 (2020).
[34] T. Soejima, D. E. Parker, N. Bultinck, J. Hauschild, and M. P. Zaletel, Efficient simulation of moiré materials using the density matrix renormalization group, Phys. Rev. B **102**, 205111 (2020).
[35] X. Zhang, G. Pan, Y. Zhang, J. Kang, and Z. Y. Meng, Momentum space quantum Monte Carlo on twisted bilayer graphene, Chin. Phys. Lett. **38**, 077305 (2021).
[36] G. Pan, X. Zhang, H. Li, K. Sun, and Z. Y. Meng, Dynamical properties of collective excitations in twisted bilayer graphene, Phys. Rev. B **105**, L121110 (2022).
[37] J. S. Hofmann, E. Khalaf, A. Vishwanath, E. Berg, and J. Y. Lee, Fermionic Monte Carlo study of a realistic model of twisted bilayer graphene, Phys. Rev. X **12**, 011061 (2022).
[38] G. Pan, X. Zhang, H. Lu, H. Li, B.-B. Chen, K. Sun, and Z. Y. Meng, Thermodynamic characteristic for a correlated flat-band system with a quantum anomalous Hall ground state, Phys. Rev. Lett. **130**, 016401 (2023).
[39] X. Zhang, G. Pan, B.-B. Chen, H. Li, K. Sun, and Z. Y. Meng, Polynomial sign problem and topological Mott insulator in twisted bilayer graphene, Phys. Rev. B **107**, L241105 (2023).
[40] A. B. Kuzmenko, I. Crassee, D. van der Marel, P. Blake, and K. S. Novoselov, Determination of the gate-tunable band gap and tight-binding parameters in bilayer graphene using infrared spectroscopy, Phys. Rev. B **80**, 165406 (2009).
[41] E. Y. Andrei and A. H. MacDonald, Graphene bilayers with a twist, Nat. Mater. **19**, 1265 (2020).
[42] Y. Xu, S. Liu, D. A. Rhodes, K. Watanabe, T. Taniguchi, J. Hone, V. Elser, K. F. Mak, and J. Shan, Correlated insulating states at fractional fillings of moiré superlattices, Nature (London) **587**, 214 (2020).
[43] Y. Saito, J. Ge, K. Watanabe, T. Taniguchi, and A. F. Young, Independent superconductors and correlated insulators in twisted bilayer graphene, Nat. Phys. **16**, 926 (2020).
[44] X. Lu, P. Stepanov, W. Yang, M. Xie, M. A. Aamir, I. Das, C. Urgell, K. Watanabe, T. Taniguchi, G. Zhang *et al.*, Superconductors, orbital magnets and correlated states in magic-angle bilayer graphene, Nature (London) **574**, 653 (2019).
[45] P. Stepanov, I. Das, X. Lu, A. Fahimniya, K. Watanabe, T. Taniguchi, F. H. Koppens, J. Lischner, L. Levitov, and D. K. Efetov, Untying the insulating and superconducting orders in magic-angle graphene, Nature (London) **583**, 375 (2020).
[46] N. N. T. Nam and M. Koshino, Lattice relaxation and energy band modulation in twisted bilayer graphene, Phys. Rev. B **96**, 075311 (2017).
[47] M. Koshino, N. F. Q. Yuan, T. Koretsune, M. Ochi, K. Kuroki, and L. Fu, Maximally localized Wannier orbitals and the extended Hubbard model for twisted bilayer graphene, Phys. Rev. X **8**, 031087 (2018).
[48] X Dai, Quantum Monte Carlo simulations in momentum space, Chin. Phys. Lett. **39**, 050101 (2022).
[49] H. Li, U. Kumar, K. Sun, and S.-Z. Lin, Spontaneous fractional Chern insulators in transition metal dichalcogenide moiré superlattices, Phys. Rev. Res. **3**, L032070 (2021).
[50] Z.-D. Song and B. A. Bernevig, Magic-angle twisted bilayer graphene as a topological heavy Fermion problem, Phys. Rev. Lett. **129**, 047601 (2022).
[51] H. Shi and X. Dai, Heavy-fermion representation for twisted bilayer graphene systems, Phys. Rev. B **106**, 245129 (2022).
[52] D. Călugăru, M. Borovkov, L. L. Lau, P. Coleman, Z.-D. Song, and B. A. Bernevig, TBG as topological heavy fermion: II. Analytical approximations of the model parameters, Low Temp. Phys. **49**, 640 (2023).
[53] H. Hu, B. A. Bernevig, and A. M. Tsvelik, Kondo lattice model of magic-angle twisted-bilayer graphene: Hund's rule, local-moment fluctuations, and low-energy effective theory, Phys. Rev. Lett. **131**, 026502 (2023).
[54] H. Hu, G. Rai, L. Crippa, J. Herzog-Arbeitman, D. Călugăru, T. Wehling, G. Sangiovanni, R. Valenti, A. M. Tsvelik, and B. A. Bernevig, Symmetric Kondo lattice states in doped strained twisted bilayer graphene, Phys. Rev. Lett. **131**, 166501 (2023).

[55] Y.-Z. Chou and S. Das Sarma, Kondo lattice model in magic-angle twisted bilayer graphene, Phys. Rev. Lett. **131**, 026501 (2023).

[56] Y. Chou and S. Das Sarma, Scaling theory of intrinsic kondo and Hund's rule interactions in magic-angle twisted bilayer graphene, Phys. Rev. B **108**, 125106 (2023).

[57] S. Liu, E. Khalaf, J. Y. Lee, and A. Vishwanath, Nematic topological semimetal and insulator in magic-angle bilayer graphene at charge neutrality, Phys. Rev. Res. **3**, 013033 (2021).

[58] K. P. Nuckolls, R. L. Lee, M. Oh, D. Wong, T. Soejima, J. P. Hong, D. Călugăru, J. Herzog-Arbeitman, B. A. Bernevig, K. Watanabe *et al.*, Quantum textures of the many-body wavefunctions in magic-angle graphene, Nature (London) **620**, 525 (2023).

[59] J. P. Hong, T. Soejima, and M. P. Zaletel, Detecting symmetry breaking in magic angle graphene using scanning tunneling microscopy, Phys. Rev. Lett. **129**, 147001 (2022).

[60] Y. H. Kwan, G. Wagner, T. Soejima, M. P. Zaletel, S. H. Simon, S. A. Parameswaran, and N. Bultinck, Kekulé spiral order at all nonzero integer fillings in twisted bilayer graphene, Phys. Rev. X **11**, 041063 (2021).

[61] T. Wang, D. E. Parker, T. Soejima, J. Hauschild, S. Anand, N. Bultinck, and M. P. Zaletel, Ground-state order in magic-angle graphene at filling $\nu = -3$: A full-scale density matrix renormalization group study, Phys. Rev. B **108**, 235128 (2023).

[62] B.-B. Chen, Y. D. Liao, Z. Chen, O. Vafek, J. Kang, W. Li, and Z. Y. Meng, Realization of topological Mott insulator in a twisted bilayer graphene lattice model, Nat. Commun. **12**, 5480 (2021).

[63] X. Lin, B.-B. Chen, W. Li, Z. Y. Meng, and T. Shi, Exciton proliferation and fate of the topological Mott insulator in a twisted bilayer graphene lattice model, Phys. Rev. Lett. **128**, 157201 (2022).

[64] A. W. Sandvik, Stochastic method for analytic continuation of quantum Monte Carlo data, Phys. Rev. B **57**, 10287 (1998).

[65] H. Shao and A. W. Sandvik, Progress on stochastic analytic continuation of quantum Monte Carlo data.

[66] H. B. Nielsen and M. Ninomiya, A no-go theorem for regularizing chiral fermions, Phys. Lett. B **105**, 219 (1981).

[67] Z. Yan and Z. Y. Meng, Relating entanglement spectra and energy spectra via path-integral on replica manifold, Nat. Commun. **14**, 2360 (2023).

[68] X. Zhang, K. Sun, H. Li, G. Pan, and Z. Y. Meng, Superconductivity and bosonic fluid emerging from moiré flat bands, Phys. Rev. B **106**, 184517 (2022).

[69] C. Zhou, Z. Yan, H.-Q. Wu, K. Sun, O. A. Starykh, and Z. Y. Meng, Amplitude mode in quantum magnets via dimensional crossover, Phys. Rev. Lett. **126**, 227201 (2021).

[70] Z. Yan, Y.-C. Wang, N. Ma, Y. Qi, and Z. Y. Meng, Topological phase transition and single/multi anyon dynamics of z_2 spin liquid, npj Quantum Mater. **6**, 39 (2021).